Experimental Mechanics
DOI 10.1007/s11340-008-9147-z

Extension of the Coherent Gradient Sensor (CGS) to the Combined Measurement of In-Plane and Out-of-Plane Displacement Field Gradients

M. Mello · S. Hong · A.J. Rosakis

Received: 20 November 2007 / Accepted: 7 April 2008

Abstract The Coherent Gradient Sensor (CGS) is extended to the optical differentiation of specular, diffracted wave fronts leading to the combined measurement of in- and out-of-plane displacement field gradients. A derivation of the underlying optical interference principles is presented along with an analysis of the effective instrument sensitivity. In order to demonstrate the capabilities of the technique, experimental measurements of crack-tip deformation fields were conducted under various loading conditions corresponding to mode-I, mode-II, and mixed mode near-tip crack fields. The experimental procedures and results of these tests are presented as validation of the technique.

Keywords Coherent Gradient Sensor (CGS) · Diffracted wave front shearing · In-plane displacement field gradients · Out-of-plane displacement field gradients · Moiré · Fine pitch grating · Ronchi grating · Phase shifting · Phase map · Crack tip deformation fields · Mode I · Mode II · Mixed mode

Introduction

The coherent gradient sensor (CGS) as originally proposed by Tippur et al., [1–7] has been previously described and successfully applied in numerous experimental stress analysis applications. Legacy CGS applications have ranged from dynamic crack-propagation studies [8–15] to the evaluation of thin film stresses on 300mm Silicon wafers [16–20]. As with all wave front shearing interferometers, CGS fringe patterns represent a spatial derivative of an optical wave front which has either been reflected or transmitted by a mechanical test specimen. The differentiated output is generally related to the physical slope of the specimen surface although it can also be related to the gradient of the sum of principle stress components when plane stress conditions prevail. In the investigation of thin film stresses, whole field plots of curvature components are obtained through the numerical differentiation of the measured slope fields.

The aforementioned legacy studies all featured a dominant out-of-plane surface slope signature which was well resolved using the conventional CGS wave front shearing arrangement. However, in cases where dominant in-plane stress fields prevail, the surface slope measurement may be a less sensitive indicator of material response. A case in point is the 2D plane stress loading arrangement which is used to simulate the rupture of a tectonic fault in Laboratory Earthquake experiments [21]. This measurement gap provides motivation for extension of the CGS technique to the whole mapping of in-plane spatial derivatives.

There is actually a fairly rich history associated with the development of wave front shearing interferometers with application to the combined whole field mapping of in- and out-of-plane displacement field gradients. The original wave front shearing interferometer designed for this purpose was developed by Hung in the early 1970s [22]. Hung's technique, and many of the early wave front shearing schemes which followed, relied upon the process of recording multiple interference patterns on a single film plate. Multiply exposed film transparencies were then post processed using optical Fourier filtering schemes in order

M. Mello (✉, SEM Member) · A.J. Rosakis (SEM Member)
Graduate Aeronautical Laboratories (GALCIT),
California Institute of Technology,
Pasadena, CA 91125, USA
e-mail: mello@caltech.edu

S. Hong
Sandia National Laboratories,
P.O. Box 0969-MS 9042, Livermore, CA 94550, USA

to extract fringe patterns corresponding to spatial derivatives of interest [22]. By the early to mid 1980s Weissman et al., [23] demonstrated whole field mapping of normal strain fields using an augmented moiré interferometer arrangement. Weissman's technique leveraged an "optical wedge" formed by a pair of uncoated optical flats in order to shear each of the normally diffracted (first order) moiré beams. The resulting interferograms, along with a superimposed carrier fringe pattern, were then sequentially recorded on the same photographic plate using a double exposure procedure. Fringe patterns corresponding to strain field components were subsequently obtained using a subtractive moiré process which served to eliminate the carrier pattern. So called "real-time optical differentiation for moiré interferometry" was later introduced by Patorski et al., [24] which featured novel polarization schemes for simultaneous wave front shearing of both moiré beams leading to the formation of additive moiré fringes of constant strain at the film plane.

With the advent of the digital age the emphasis quickly shifted away from the use of film based methods in favor of the CCD camera which enables digital recording of fringe patterns with the aid of a personal computer and an integrated frame grabber board. Enabled by the rapid advancement and commercial availability of the PC, phase shifting interferometry (PSI) emerged as the prevailing method for processing and analyzing fringe patterns [25–27]. PSI techniques depend upon a series of phase shifted fringe patterns which are generated through the precise mechanical translation of an optical component. Controlled displacements are usually achieved with the aid of a small stepper motor or piezoelectric transducer. Other PSI schemes feature the novel use of polarization components or even direct modulation of the light source in order to induce a desired phase shift [28]. A simple point by point calculation is then applied in order recover the wave front phase information which is encoded within the intensity variations contained within the sequence of phase shifted fringe patterns. The earliest application of the PSI method to the combined measurement of in- and out-of-plane displacement field gradients traces back to work by Nakadate et al., [29]. The approach was subsequently refined over the years through the work of Rastogi [30], and numerous other researchers with primary emphasis on the development and application of electronic speckle pattern shearing interferometers (ESSPI).

CGS Diffracted Wave Front Shearing Arrangement

The CGS diffracted wave front configuration is depicted in Fig. 1. A two-dimensional (crossed) specimen grating is illuminated by a pair of obliquely incident beams in either the x_1–x_3 or x_2–x_3 planes using a traditional moiré interferometer arrangement. Sharp diffraction orders arise which propagate within each respective plane of incidence. The diffraction angles are given by the general grating equation

$$\sin\theta_m = \sin\theta_i + m\frac{\lambda}{d} \tag{1}$$

where λ represents the laser wavelength, d equals the pitch of the undeformed specimen grating, Θ_i represents the angle of incidence, m = 0, +/−1, +/−2, … +/−k designates the diffraction order, and Θ_m represents the corresponding diffraction angle. Each illuminating beam is precisely adjusted in order to satisfy the first order diffraction angle condition of the fine pitch grating given by

$$\sin\Theta_i = \frac{\lambda}{d} \tag{2}$$

Figure 2 depicts how each illuminating beam gives rise to a first-order diffracted beam which emerges normal to the surface of the specimen. The normally diffracted beams are paired to-

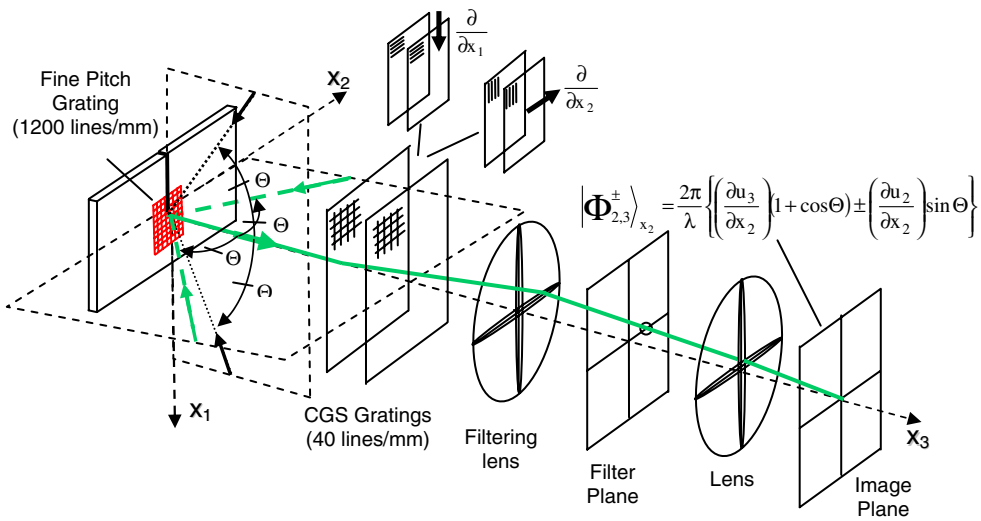

Fig. 1 CGS diffracted wave front shearing configuration

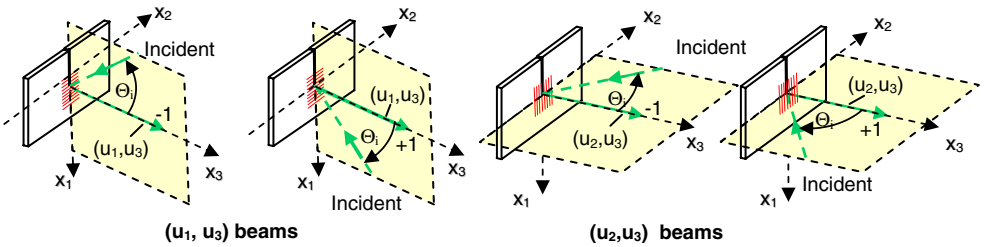

Fig. 2 (u_1,u_3) beams comprised of +1 and −1 diffracted orders in the x_1–x_3 plane and the (u_2,u_3) beams comprised of +1 and −1 diffracted orders in the x_2–x_3 plane

gether and designated as the (u_1,u_3) beam pair and the (u_2,u_3) beam pair respectively, in order to distinguish the plane of incidence and the specific combination of in-plane and out-of-plane displacement field components which are encoded into each diffracted wave front.

The working principle of the CGS diffracted wave front shearing arrangement is explained by invoking a simple ray optics model as depicted in Fig. 3. The obliquely incident beams are each diffracted by the reflective specimen grating G_0. An optical shutter or simple beam stop is used to temporarily block one of the incident beams in order to prevent interference between the +1 and −1 normally diffracted orders. Next, we consider a pair of neighboring points a and b on the specimen surface which are separated by a lateral (shearing) distance (s_2) as shown. The light ray which originates at point a is normally transmitted through the first CGS Ronchi grating G_1 and then diffracted as a 1st order ray by the CGS Ronchi grating G_2. A second light ray, which emerges from the neighboring point b is diffracted as a 1st order ray by the CGS Ronchi grating G_1 and then transmitted straight through the CGS Ronchi grating G_2. The two rays then merge as they exit from grating G_2. This simple ray optics picture applies to the continuum of all such pairs of neighboring points across the illuminated specimen surface and forms the basis of the CGS scheme. From a wave front perspective, the Ronchi gratings serve to generate two laterally offset (sheared) copies of the original diffracted wave front. The sheared wave fronts mutually interfere as they emerge from grating G_2 and the resulting fringe pattern is modulated by the optical path length differences which arise as the specimen deforms. (s_2) thus represents a natural gage length across which a displacement gradient is obtained. In general, the lateral shearing distance (s_β) is controlled by the Ronchi grating pitch (p) and grating separation (Δ) and is given by

$$S_\beta = \Delta\frac{\lambda}{p} \quad (\beta = 1,2) \tag{3}$$

where β = 1,2 denotes lateral shearing with respect to the x_1 and x_2 directions, respectively. Wave front shearing with respect to the x_1 direction is achieved by simply rotating each Ronchi grating by 90°.

Numerous additional diffraction orders (not depicted in Fig. 3) are also generated by G_1 and G_2 in accordance with equation (1). A focusing lens L and spatial filtering mask A are used to suppress these extraneous diffraction orders while facilitating passage of the laterally sheared 1st order wave fronts which emerge from G_2. The resulting fringe pattern is then focused onto the image plane I and captured using a CCD camera with integrated phase shifting diagnostics. Once a sequence of phase shifted images is acquired, the illuminating beam is blocked and the procedure is repeated with the second illuminating beam. The complementary phase information obtained from these two independent wave front shearing operations is subsequently combined to generate de-coupled whole field plots of the in- and out-of-plane displacement field gradients.

Interference of Laterally Sheared Diffracted Wave Fronts

Without any loss of generality, the interference problem is derived by considering wave front shearing of the normally diffracted (u_2, u_3) beams with respect to the x_2 direction. Results of the derivation are then generalized to any beam

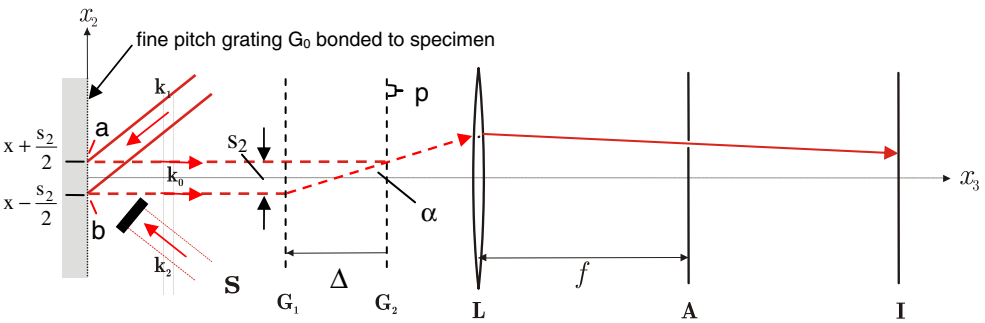

Fig. 3 Working principle of the in-plane and out-of-plane sensitive CGS setup

pair (u_α, u_3) [α = 1,2] and wave front shearing direction x_β [β = 1,2]. Figure 4 depicts how the optical path lengths of the normally diffracted wave fronts are perturbed as an arbitrary point a, located at coordinate (x_1,x_2 + S_2 / 2), suffers an in-plane displacement to a point a' and an out-of-plane displacement to a point a''.

A similar argument applies to the displacements at the neighboring point b which is located at coordinate (x_1, $x_2 - x_2$ / 2; not depicted in Fig. 4). The resulting change in path length (δS) of a diffracted ray in response to the displacements at each of these two neighboring points is given by

$$\underbrace{\delta S\left(x_1, x_2 + \frac{s_2}{2}, t\right)}_{\text{point a}} = u_3\left(x_1, x_2 + \frac{s_2}{2}, t\right)[1 + \cos\Theta] \pm \left(u_2\left(x_1, x_2 + \frac{s_2}{2}, t\right)\sin\Theta\right) \tag{4a}$$

$$\underbrace{\delta S\left(x_1, x_2 - \frac{s_2}{2}, t\right)}_{\text{point b}} = u_3\left(x_1, x_2 - \frac{s_2}{2}, t\right)[1 + \cos\Theta] \pm \left(u_2\left(x_1, x_2 - \frac{s_2}{2}, t\right)\sin\Theta\right) \tag{4b}$$

where the +/− symbols are associated with the +1 and −1 diffracted orders in accordance with Fig. 4. The laterally displaced wave fronts are modeled as plane waves given by

$$E_a = E\left(x_1, x_2 - \frac{s_2}{2}, t\right) = A\exp i\left\{kx_3 - \omega t - \frac{2\pi}{\lambda}\left(\delta S\left(x_1, x_2 - \frac{s_2}{2}, t\right)\right\}\right. \tag{5a}$$

$$E_b = E\left(x_1, x_2 + \frac{s_2}{2}, t\right) = A\exp i\left\{kx_3 - \omega t - \frac{2\pi}{\lambda}\left(\delta S\left(x_1, x_2 + \frac{s_2}{2}, t\right)\right\}\right. \tag{5b}$$

in accordance with the coordinate description of Fig. 3. Here, A and B represent arbitrary plane wave amplitudes, $k = 2\pi / \lambda$ is the wave number, x_3 represents the propagation distance to the image plane, and t represents time. The

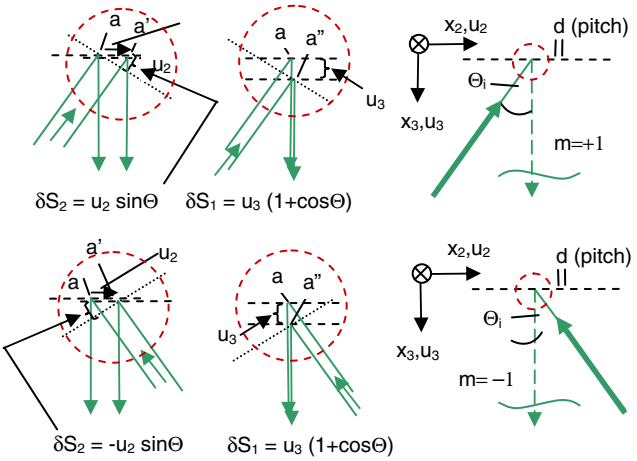

Fig. 4 Geometric representation of the optical path length changes induced by in-plane and out-of-plane displacements as the specimen grating undergoes deformation

interference problem is solved by taking the time averaged intensity of the combined plane wave fields given by

$$I \infty \{E_a + E_b\}\{E_a + E_b\}^* \tag{6}$$

where the symbol * denotes the complex conjugate operation and the optical constants of proportionality are suppressed. This leads directly to the familiar two beam interference expression given by

$$I(x_1, x_2, t) = I_a + I_b + 2\sqrt{I_a I_b}\cos\frac{2\pi}{\lambda}\left[\lim_{s\to 0}\left(\delta S\left(x_1, x_2 + \frac{s_2}{2}, t\right) - \delta S\left(x_1, x_2 - \frac{s_2}{2}, t\right)\right)\right] \tag{7}$$

where I_a and I_b represent the constant background intensity of each laterally sheared beam. The third term represents the interference which modulates in response to the *differential displacement* between pairs of neighboring points separated by the lateral shearing distance s_2. The result is expressed here in limit form in order to emphasize the fact that (I) can only approximate the time averaged intensity at the point (x_1, x_2) in the limit that the shearing distance (s_2) is made sufficiently small. Substituting the optical path length expressions (4a) and (4b) into equation (7) yields an expanded representation of the differential phase term given by

$$\left|\Psi^{+/-}_{\alpha,3}\right\rangle_{x_2} = \lim_{s_2\to 0}\frac{2\pi}{\lambda}\left\{\left(u_3\left(x_1, x_2 + \frac{s_2}{2}, t\right) - u_3\left(x_1, x_2 - \frac{s_2}{2}, t\right)\right)(1 + \cos\Theta) \pm \left(u_\alpha\left(x_1, x_2 + \frac{s_2}{2}, t\right) - u_\alpha\left(x_1, x_2 - \frac{s_2}{2}, t\right)\right)\sin\Theta\right\} \tag{8}$$

Note that the symbols $\left|\Psi^{+/-}_{2,3}\right\rangle_{x_2}$ are used to denote lateral shearing of the (u_2,u_3) beam pair with respect to the (x_2) direction and that the +/− sign is used to specify the +1 or −1 diffraction order.

Repeated application of the two beam interference problem with respect to the x_1 shearing direction or to the (u_2,u_3) beam pair, along either shearing direction leads to a general result given by

$$\left|\Psi_{\alpha,3}^{+/-}\right\rangle_{x_\beta} = \lim_{s_\beta \to 0} \frac{2\pi}{\lambda}\left\{\left(u_3\left(x_1, x_2+\frac{s_\beta}{2}, t\right) - u_3\left(x_1, x_2-\frac{s_\beta}{2}, t\right)\right)(1+\cos\Theta) \pm \left(u_\alpha\left(x_1, x_2+\frac{s_\beta}{2}, t\right) - u_\alpha\left(x_1, x_2-\frac{s_\beta}{2}, t\right)\right)\sin\Theta\right\} \tag{9}$$

where α = 1,2 denotes the in-plane displacement field component and β = 1,2 specifies the wave front shearing direction. Moreover, since we are primarily interested in spatial derivatives of the diffracted wave fronts, it is natural to recast equation (9) in differential form given by equation (10) which applies in the limit where the shearing distance (s_β) is sufficiently small in comparison to the characteristic length scales of interest. The general phase term expressed by equation (10) represents a total of eight possible phase maps which may be obtained through lateral shearing of the four

$$\left|\Phi_{\alpha,3}^{+/-}\right\rangle_{x_\beta} = \frac{2\pi}{\lambda}\left\{\left(\frac{\partial u_3(x_1,x_2,t)}{\partial x_\beta}\right)(1+\cos\Theta) \pm \left(\frac{\partial u_\alpha(x_1,x_2,t)}{\partial x_\beta}\right)\sin\Theta\right\}\frac{1}{s_\beta}\left|\Psi_{\alpha,3}^{+/-}\right\rangle_{x_\beta} \quad \alpha = 1,2;\ \beta = 1,2 \tag{10}$$

(u_α,u_3) diffracted wave fronts with respect to two primary shearing directions. Wave front shearing along other off-axis directions, while certainly possible and physically meaningful in certain applications, is not considered. Perhaps most importantly, the form of equation (10) reveals how de-coupling of the in-plane and out-of-plane displacement field gradient terms may be achieved through the addition or subtraction of symmetric m = ±1 phase terms with the aid of PSI techniques.

De-coupling the In- and Out-of-Plane Displacement Field Gradients

Temporal PSI techniques offer a powerful and convenient means of extracting whole field phase information in quasi-static testing applications. Phase shifting of CGS fringe patterns is facilitated by a calibrated PZT actuator which is used to induce a series of incremental transverse movements of one Ronchi grating with respect to the other (along a direction perpendicular to the grating lines). A sequence of phase shifted fringe patterns is acquired from each of the laterally sheared wave fronts. A corresponding phase shifting algorithm is then applied in order to extract the wrapped phase information.

Derivatives of Out-of-Plane Displacement Fields (Surface Slope)

The addition of complementary phase map pairs as expressed by equation (10) induces a complete cancellation of the in-plane displacement gradient term and produces a de-coupled whole field phase map of the surface slope components given by

$$\left|\Phi_{\alpha,3}\right\rangle_{x_\beta} + \left|\Phi_{\alpha,3}\right\rangle_{x_\beta} = \frac{4\pi}{\lambda}\left\{\left(\frac{\partial u_3(x_1,x_2,t)}{\partial x_\beta}\right)(1+\cos\Theta)\right\} \quad \alpha = 1,2;\ \beta = 1,2 \tag{11}$$

As with all lateral shearing interferometers, the CGS wave front shearing scheme is naturally self referencing by nature, i.e. interference is preserved through moderate rigid body rotations since the interfering (sheared) beams move together as the specimen surface tilts. Moreover, there is no signature fringe pattern which results from sheared, tilted wave fronts since the shape of a diffracted wave front remains largely unaffected by small perturbations in the angle of incidence.

The use of a 2D (crossed line) fine pitch diffraction grating on the specimen surface enables two independent measurements of the same surface slope component. For example, the $\frac{\partial u_3}{\partial x_1}$ surface slope component may be obtained by shearing the (u_1,u_3) diffracted beam pair with respect to the x_1 direction and then adding the corresponding phase maps as follows

$$\frac{\partial u_3(x_1,x_2,t)}{\partial x_1} = \frac{\lambda}{4\pi(1+\cos\Theta)}\left|\Phi_{1,3}^{+}\right\rangle_{x_1} + \left|\Phi_{1,3}^{-}\right\rangle_{x_1} \tag{12}$$

Alternatively, the same slope component may be obtained using a pair of orthogonally oriented illuminating beams in the x_2–x_3 plane. In the latter case, lateral wave front

shearing of the (u_2,u_3) diffracted beam pair with respect to the x_1 direction, followed by addition of the complementary phase maps, leads to a surface slope measurement given by

$$\frac{\partial u_3(x_1,x_2,t)}{\partial x_1} = \frac{\lambda}{4\pi(1+\cos\Theta)}\left|\Theta^+_{2,3}\right\rangle_{x_1} + \left|\Theta^-_{2,3}\right\rangle_{x_1} \tag{13}$$

Likewise, two independent measurements of the orthogonal $-\frac{\partial u_3}{\partial x_2}$ surface slope component may also be obtained through wave front shearing and subsequent addition of corresponding (u_1,u_3) or (u_2,u_3) phase terms. The slope measurements expressed by equations (12) and (13) are not redundant measurements but instead represent a unique situation where two independent measurements of the same quantity can be obtained by sampling the specimen surface with different pairs of illuminating beams.

The process of adding complementary phase maps in accordance with equation (10) also leads to an increased overall measurement sensitivity as compared to conventional surface slope measurements obtained through lateral shearing of a normally reflected wave front. A more detailed discussion of effective instrument sensitivity to changes in surface slope is discussed in a later section.

Derivatives of In-Plane Displacement Fields (Strain Fields)

The subtraction of complementary phase map pairs as expressed by equation (10) induces a complete cancellation of the out-of-plane displacement gradient term. This results in a de-coupled phase map corresponding to a spatial derivative of the in-plane displacement field which is given by

$$\left|\Phi^+_{\alpha,3}\right\rangle_{x_\beta} - \left|\Phi^-_{\alpha,3}\right\rangle_{x_\beta} = \frac{4\pi}{\lambda}\left\{\left(\frac{\partial u_\alpha(x_1,x_2,t)}{\partial x_\beta}\right)\sin\theta\right\} \qquad \alpha = 1,2;\ \beta = 1,2 \tag{14}$$

The procedure leads directly to the whole field mapping of infinitesimal strain components in the limit where the shearing distance is deemed sufficiently small in comparison to the characteristic length scale of interest. Note that whole field plots obtained in this manner represent a change in strain between the deformed and reference configurations which does not necessarily correspond to the absolute state of strain in the specimen.

By appealing to equation (1) it is easy to see how a uniform extension or contraction of the specimen grating pitch (d) will simply alter the propagation vector of an otherwise planar diffracted wave front. In other words the diffraction angle is perturbed but there is no distortion of the optical wave front. Consequently, there is a subtle measurement ambiguity associated with the measurement of homogenous deformations. Indeed this is the in-plane analog to the manner in which traditional wave front shearing interferometers, which measure surface slope, are insensitive to rigid body tilt of the specimen surface. In cases where homogeneous in-plane deformations are suspected or encountered, Moiré interferometry can also be leveraged by simply removing one of the Ronchi gratings and simply allowing the +1 and −1 diffracted orders to mutually interfere. Independent measurements of the u_1 and u_2 displacement fields may be used to supplement the CGS data and vice versa. In this way the two techniques become quite complementary. Most problems of interest however, will generally exhibit some degree of inhomogeneous deformation and the issue of a constant strain measurement ambiguity is seldom encountered. Nonetheless, one should be mindful of this issue when applying the technique and interpreting results.

Effective Instrument Sensitivity

The method of obtaining displacement field gradients through the linear combination of phase information as expressed by equations (11) and (14) is tantamount to having two independent "virtual" lateral shearing interferometers working in tandem, one of which outputs surface slope information and a second which yields in-plane displacement field gradients (or strain fields in the limiting case where the shearing distance is deemed sufficiently small). In the spirit of this model, we can postulate the existence of a "virtual" fringe pattern associated with each decoupled phase term in order to derive expressions for the effective measurement sensitivity.

Sensitivity to the Measurement of Surface Slopes

Fringes orders defining iso-contours of surface slope are defined by considering a $2\pi N$ phase change in equation (11), where N is an integer corresponding to an arbitrary fringe order. The change in surface slope per fringe order, i.e., the effective instrument sensitivity, is then given by

$$\frac{1}{N}\frac{\partial u_3(x_1,x_2,t)}{\partial x_\beta} = \frac{1}{s_\beta}\left\{\frac{\lambda}{2(1+\cos\Theta)}\right\} \quad \beta = 1,2 \tag{15}$$

The presence of the (1 + cosΘ) factor in the denominator reveals an increased sensitivity compared to surface slope measurements obtained using a conventional wave front shearing interferometer. This results from the fact that the surface is sampled by two oblique illuminating beams in the diffracted wave front shearing case as opposed to a single, normally incident, illuminating beam in the case of a conventional wave front shearing interferometer. Indeed, it is interesting to note how the limiting sensitivity value of $\frac{\lambda}{4s_\beta}$ in equation (15) is equivalent to doubling the number of reflections in a conventional wave front shearing interferometer

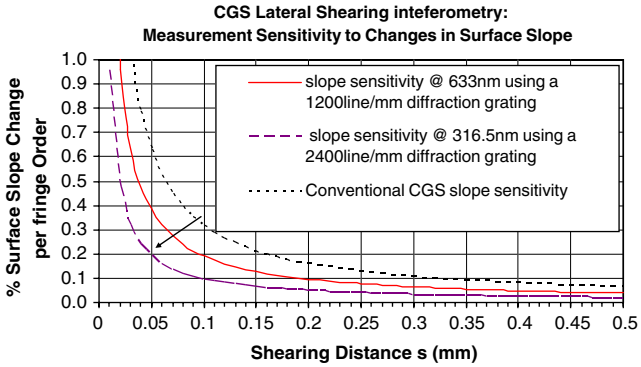

Fig. 5 Plots of effective instrument sensitivity to changes in surface slope as a function of the lateral shearing distance (s)

operating at normal incidence. Figure 5 is a plot of the effective instrument sensitivity to changes in surface slope as a function of the lateral wave front shearing distance (s_β). The arrow in the figure highlights the trend of increased instrument sensitivity between the three cases which are considered. The uppermost curve is a plot of the measurement sensitivity in the case of a conventional CGS operating at a laser wave length of 633nm. The middle curve displays the increased sensitivity which results from the addition of complementary phase terms using the diffracted wave front shearing technique. The lowermost curve correspond to an extreme limiting case outside of the visible light range at an operating wavelength of 316.5nm (ultra-violet) with a 2400 line/mm grating where the source wavelength and specimen grating pitch have been both reduced by one-half in order to hold the diffraction angle Θ constant.

An alternative form for the effective instrument sensitivity, expressed purely in terms of instrument parameters, is given by

$$\frac{1}{N}\frac{\partial u_3(x_1,x_2,t)}{\partial x_\beta} = \frac{p}{2\Delta}\left\{1+\sqrt{1-\left(\frac{j\lambda}{d}\right)^2}\right\}^{-1} \quad \beta = 1,2 \tag{16}$$

where (j) represents the diffraction order (typically j=+/−1)

Sensitivity to the Measurement of Surface Strains

A similar approach is applied to determine the effective instrument sensitivity to changes in surface strain. Fringes orders defining strain iso-contours are defined by considering a $2\pi N$ phase change in equation (14), where N is an integer corresponding to an arbitrary fringe order. The change in strain per fringe order is expressed by

$$\frac{1}{N}\frac{\partial u_\alpha(x_1,x_2,t)}{\partial x_\beta} = \frac{1}{s_\beta}\left\{\frac{\lambda}{2\sin\Theta}\right\} \quad \alpha = 1,2;\ \beta = 1,2 \tag{17}$$

Instrument sensitivity is seen to range from a maximum sensitivity value of $\frac{\lambda}{2s_\beta}$ at the (impractical) grazing incidence case where the illumination angles approach 90°, to infinity in the limit of extremely shallow illumination angles approaching 0°, in which case the interferometer is rendered completely insensitive. As a point of reference, it is common practice to employ a grating frequency of 1,200line/mm in which case the 1st order diffraction angle equals ~49.4° for a laser wavelength of λ = 633nm. In this case the sensitivity relation given by equation (17) reveals that the instrument is already operating at 76% of its theoretical limiting value for a given shearing distance. There are clearly diminished returns which result from simply increasing the specimen grating frequency when operating at a given fixed wave length. The graph in Fig. 6 displays a plot of instrument sensitivity to changes in surface strain plotted as a function of shearing distance s_β. The uppermost curve corresponds to the diffracted wave front shearing measurement and the subtraction of the complementary phase terms. The lower curve once again corresponds to an extreme limiting condition at the 316.5nm UV wavelength whereby the source wavelength and specimen grating pitch are both reduced by one-half in order to hold the diffraction angle constant. The sensitivity relationship can also be expressed in terms of the specimen grating pitch (d) by substituting for Θ through equation (2) in which case the effective instrument sensitivity to changes in surface strain is given by

$$\frac{1}{N}\frac{\partial u_\alpha(x_1,x_2,t)}{\partial x_\beta} = \frac{1}{s_\beta}\left\{\frac{d}{2j}\right\} \quad \alpha = 1,2;\beta = 1,2 \tag{18}$$

Note how the effective instrument sensitivity per unit shearing distance, is equivalent, as it should be, to the fundamental in-plane displacement sensitivity of a conventional moiré interferometer [31] and other diffraction grating based interferometers such as the transverse displacement interferometer (TDI) [32, 33]. A third form, expressed purely in terms of CGS instrument parameters, is obtained by substituting for the shearing distance (s_β) using equation (3).

$$\frac{1}{N}\left(\frac{\partial u_\alpha(x_1,x_2,t)}{\partial x_\beta}\right) = \frac{p}{2j\Delta}\left\{\frac{d}{\lambda}\right\} \quad \alpha = 1,2;\ \beta = 1,2 \tag{19}$$

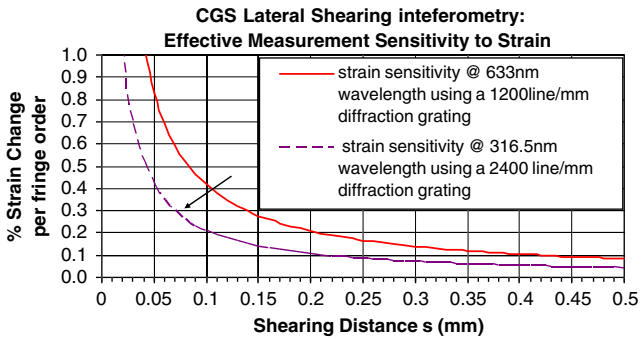

Fig. 6 Plots of effective instrument sensitivity to changes in strain expressed as a function of the lateral shearing distance (s)

Application to Crack-Tip Deformation Fields

Experimental measurements of crack-tip deformation fields corresponding to mode-I, mode-II, and mixed mode near-tip crack fields were conducted using symmetric and asymmetric four bend loading configurations. The symmetric and asymmetric loading configurations corresponding to the four-point bending fracture tests used in this study are depicted in Fig. 7.

Since the beam is assumed to be under static equilibrium, the shear force Q, (between the inner loading points), the bending moment M, and applied load P are related by

$$Q = P\left(\frac{b_2 - b_1}{b_1 + b_2}\right) M = cQ \tag{20}$$

The mode-I, mode-II, and mixed-mode, asymptotic crack-tip fields are characterized by three different values of mode mixity ($\Psi = 0°, 90°, 45°$) defined by

$$\Psi = \tan^{-1}\left(\frac{K_{II}}{K_I}\right) \tag{21}$$

where K_I and K_{II} correspond to mode-I and mode-II stress intensity factors, respectively. Following Tada et al., [34], the stress intensity factor corresponding to the pure mode I loading case, as depicted in Fig. 7(a), is given by

$$K_I = 3.975\frac{M}{a^{3/2}} \tag{22}$$

The resulting u_1, u_2, and u_3 displacement fields under plane stress *mode-I* loading conditions are given by

$$u_1 = \frac{K_I}{\mu}[r/(2\pi)]^{1/2}\cos\frac{\theta}{2}\left[1 - \frac{2\upsilon}{1+\upsilon} + \sin^2\frac{\theta}{2}\right] \tag{23}$$

$$u_2 = \frac{K_I}{\mu}[r/(2\pi)]^{1/2}\sin\frac{\theta}{2}\left[1 - \frac{2\upsilon}{1+\upsilon} + \cos^2\frac{\theta}{2}\right] \tag{24}$$

$$u_3 = \frac{-\upsilon h}{E}\frac{K_I}{(2\pi r)^{1/2}}\cos\left(\frac{\theta}{2}\right) \tag{25}$$

Following He and Hutchinson [35], the mode-I and mode-II stress intensity factors corresponding to the asymmetric four point bend loading arrangement depicted in Fig. 7(b) are expressed as

$$K_I = \frac{6cQ}{W^2}\sqrt{\pi a}F_1(a/W) \tag{26}$$

$$K_{II} = \frac{Q}{W^{1/2}}\frac{(a/W)^{3/2}}{(1-a/W)^{1/2}}F_{II}(a/W) \tag{27}$$

where the shape factors F_I (a / W) and F_{II} (a / W) are given by

$$F_I(a/W) = 1.122 - 1.121\left(\frac{a}{W}\right) + 3.740\left(\frac{a}{W}\right)^2 + 3.783\left(\frac{a}{W}\right)^3 - 19.05\left(\frac{a}{W}\right)^4 + 22.55\left(\frac{a}{W}\right)^5 \left[\frac{a}{W} \le 0.7\right] \tag{28}$$

$$F_{II}(a/W) = 7.264 - 9.37\left(\frac{a}{W}\right) + 2.74\left(\frac{a}{W}\right)^2 + 1.87\left(\frac{a}{W}\right)^3 - 1.04\left(\frac{a}{W}\right)^4 \left[0 \le \frac{a}{W} \le 1\right] \tag{29}$$

Under pure mode-II loading conditions, the plane stress predictions for the u_1, u_2, and u_3 displacement fields are given by

$$u_1 = \frac{K_{II}}{\mu}[r/(2\pi)]^{1/2}\sin\frac{\theta}{2}\left[2 - \frac{2\upsilon}{1+\upsilon} + \cos^2\frac{\theta}{2}\right] \tag{30}$$

$$u_2 = \frac{K_{II}}{\mu}[r/(2\pi)]^{1/2}\cos\frac{\theta}{2}\left[-1 + \frac{2\upsilon}{1+\upsilon} + \sin^2\frac{\theta}{2}\right] \tag{31}$$

$$u_3 = \frac{\upsilon h}{E}\frac{K_{II}}{(2\pi r)^{1/2}}\sin\left(\frac{\theta}{2}\right) \tag{32}$$

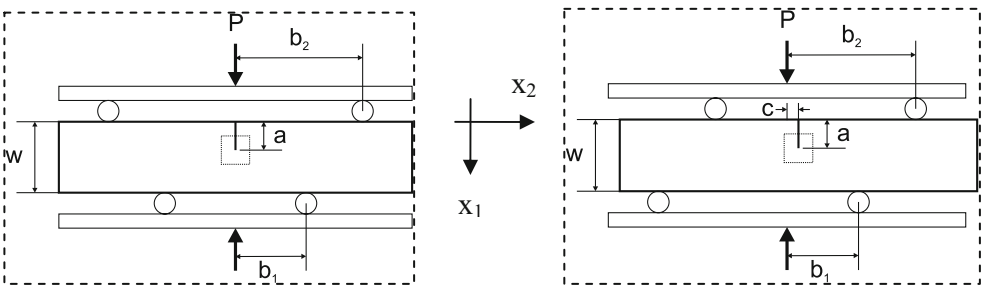

(a) Symmetric four-point bending (b) Asymmetric four-point bending

Fig. 7 Four-point bending fracture test setups and specimens (a=10 mm, b_1=25 mm, b_2= 45 mm)

Experimental Procedure

Brittle polyester resin (Homalite-100) was used as a model material for measuring in-plane and out-of-plane displacement gradient fields near a notch tip. A single-edge-notched specimen was machined from a Homalite-100 sheet (thickness, h = 4.66mm) having a notch width of 250μm. A diffraction grating with a groove frequency of 1,200lines/mm was replicated onto the specimen surface using established grating replication techniques [31]. The specimen was illuminated by two oblique, expanded, and properly collimated laser beams of wavelength, λ = 0.633μm. Precise alignment of the optical configuration was achieved through the temporary establishment of moiré null field fringe patterns using the same master grating element from which the specimen replica grating was obtained. A CGS lateral shearing interferometer was then assembled using two linear Ronchi gratings G_1 and G_2 with a line pair frequency of 40lines/mm, an imaging lens L of focal length f = 300mm, and a circular filtering aperture A (diameter, D = 5mm) at the focal plane of the lens L, in accordance with Fig. 3. A square region (10mm × 10mm) surrounding the notch tip was chosen as a field of view for the measurements. An instrument grating spacing of Δ = 20mm resulted in a lateral shearing distance of 0.5mm. The resulting fringe patterns were focused onto the image plane and recorded using a digital CCD camera (Uniq Vision, Inc., UP-1030) with a resolution of 1,024 × 1,024 pixels. A three-step phase-shifting technique was employed by translating one of the diffraction gratings with respect to the other using a PZT actuator (Physik Instrumente, P-840.10). The phase shifting device was precisely calibrated in order to eliminate any phase shift errors introduced PZT non-linearity and other sources of phase shift error. Once the optical configuration was precisely aligned and phase shifting diagnostics calibrated, the master grating element was removed and replaced by a test specimen within a miniature load frame assembly.

Three fracture tests were conducted which involved static notches loaded to produce mode-I, mode-II, and mixed-mode asymptotic crack-tip fields which can be characterized by three different values of mode mixity (Ψ = 0°, 90°, 45°). In all threes cases, load levels were monitored using a calibrated miniature load cell and test loads were maintained well within the elastic range of the highly brittle Homalite specimen.

A set of three phase-shifted interferograms were recorded from each of the sheared +1 and −1 diffracted orders prior to the application of any load in order to establish baseline data corresponding to the undeformed configuration. A set of three phase-shifted interferograms were then obtained from each of the sheared diffracted beams at the subsequent load steps. Wrapped phase maps were then generated from each set of phase shifted fringe patterns using a three step PSI algorithm [26, 27]. Phase maps corresponding to the undeformed configuration were subtracted from corresponding "deformed" phase maps acquired after loading in order to eliminate background noise due to surface imperfections within the specimen grating and dust particles on the optical components. Surface slope and strain field plots were then obtained from the filtered phase maps in accordance with equations (11) and (14).

Results: Mode-I Crack Tip Fields

The four interferograms depicted in Fig. 8 were acquired through lateral shearing of the (u_2,u_3) diffracted orders while the test specimen was subjected to a symmetric *mode-I* near-tip loading condition (P = 100N, Ψ = 0°). Interferograms 8a and 8b resulted from wave front shearing with respect to the x_2-direction (perpendicular to the notch direction). Figure 8(a) corresponds to the sheared +1 diffraction order and Fig. 8(b) corresponds to the sheared −1 diffraction order. A second pair of interferograms depicted in 8c and 8d resulted from wave front shearing with respect to the x1-direction (parallel to the notch direction) after simply rotating Ronchi gratings by 90°. Note how the fringe patterns comprising each image pair are nearly mirror images of one another with respect to the x_1 axis due to the anti-symmetric character of the u_2 displacement field i.e., $u_2(x_1,x_2) = -u_2(x_1,x_2)$. Figure 9 depicts a Moiré fringe pattern of the u_2 displacement field which was obtained by

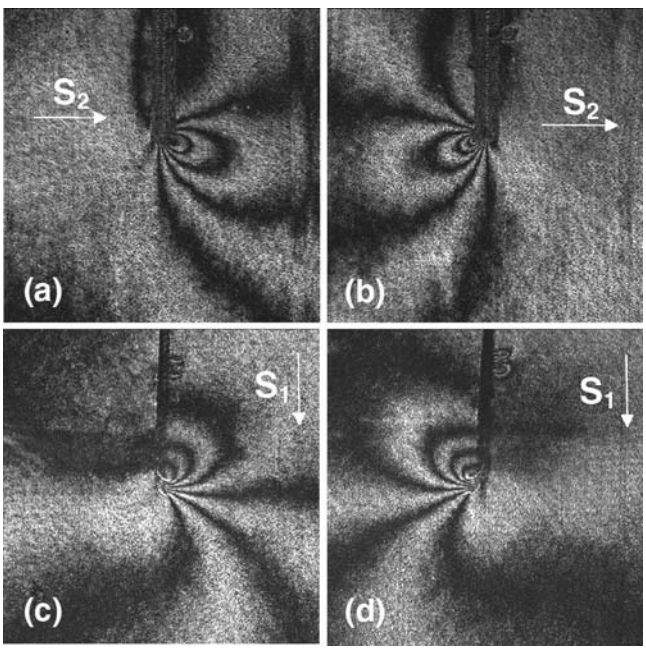

Fig. 8 Mode-I loading conditions (P=100 N, ψ=0°). CGS interferograms obtained through lateral shearing of the (u_2,u_3) diffracted orders along the x_1 and x_2 directions

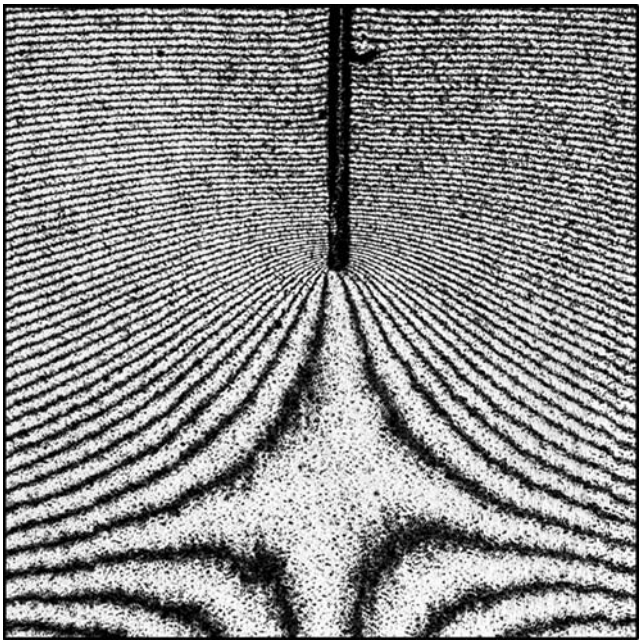

Fig. 9 Moiré interferometry fringes of displacement field u_2 corresponding to pure mode-I loading conditions

simply removing one of the double gratings in the CGS set up and allowing the +1 and −1 diffracted orders to mutually interfere. In this case each fringe order corresponds to an in-plane displacement of 0.417μm. The anti-symmetric character of the u_2 displacement field is evident.

A sequence of three phase shifted fringe patterns was obtained for each of the interferograms depicted in Fig. 8. Images were subsequently processed in order to generate a wrapped phase map of each differentiated wave front. The wrapped 2π-modulo phase maps corresponding to the interferograms in Figs. 8(a) and 8(b) are displayed in Fig. 10, each of which corresponds to a linear combination of in- and out-of-plane displacement field gradients in accordance with equation (10).

Following this step, the corresponding surface slope and strain fields were obtained by addition and subtraction of the complementary phase maps in accordance with equations (11) and (14). Figure 11(a) corresponds to a whole field phase map of the infinitesimal ε_{22} strain component obtained through subtraction of the complementary phase maps shown in Fig. 10. Here, each 2π-phase fringe corresponds to a strain difference of 8.36×10^{-4}. Figure 11(b) corresponds to a whole field phase map of the surface slope component obtained through addition of the same two phase terms. Here each 2π-phase fringe represents a slope difference of 3.85×10^{-4}. Synthetically generated plots of the corresponding displacement field gradients, obtained through differentiation of the asymptotic crack-tip K_I displacement field solutions (24) and (25) are shown in Figs. 11(c) and 11(d) for the sake of comparison. The general shape and orientation of the measured surface slope and strain fields appear to be in good agreement with the corresponding synthetically generated profiles. The discrepancy in the fringe shapes especially in the slope map in the crack-flank area is due to the truncation of higher order terms in the analytical solution as well as the effect of a finite notch width. Continuous maps of the strain and the slope fields (not depicted) were also obtained for quantitative deformation analysis. Angular variations of the ε_{22} strain component around the crack tip were evaluated along circular paths for three different radii (r/h = 0.25, 0.5, 1.0) which were normalized with respect to the thickness of the specimen h. The plot in Fig. 12 shows that the angular strain distributions are self-similar with minor variations within the experimental scatter.

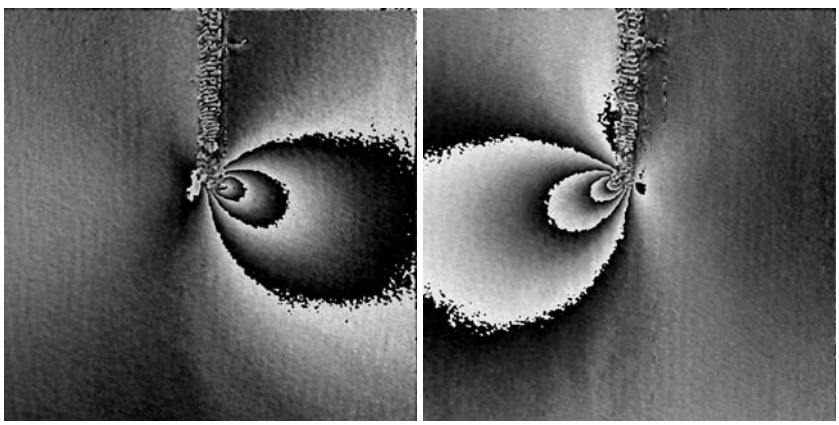

$$\frac{\lambda}{2\pi}\left|\Phi^{+}_{2,3}\right\rangle_{x_2} = \sin\theta\frac{\partial u_2}{\partial x_2} + (1+\cos\Theta)\frac{\partial u_3}{\partial x_2} \quad \frac{\lambda}{2\pi}\left|\Phi^{+}_{2,3}\right\rangle_{x_2} = \sin\theta\frac{\partial u_2}{\partial x_2} + (1+\cos\Theta)\frac{\partial u_3}{\partial x_2}$$

Fig. 10 Complementary phase maps resulting from optical differentiation of the +1 and −1 diffracted orders comprising the (u_2,u_3) beams

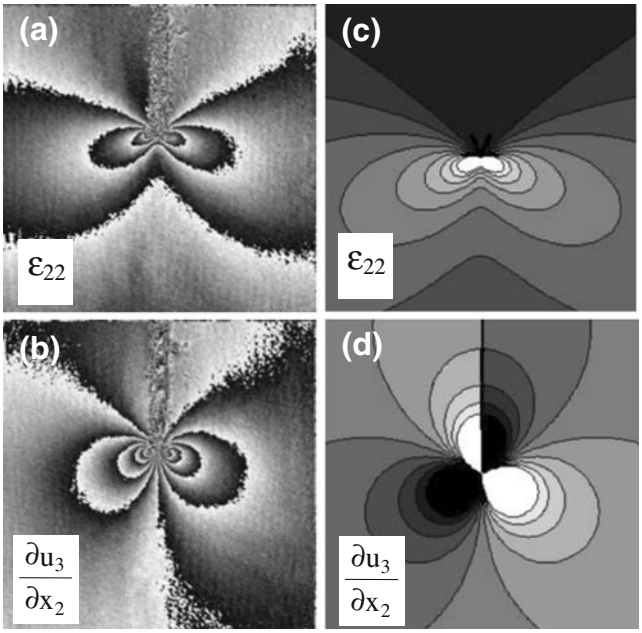

Fig. 11 Measured versus predicted crack-tip deformation fields corresponding to pure mode-I loading condition (P=100N, Ψ=0°).

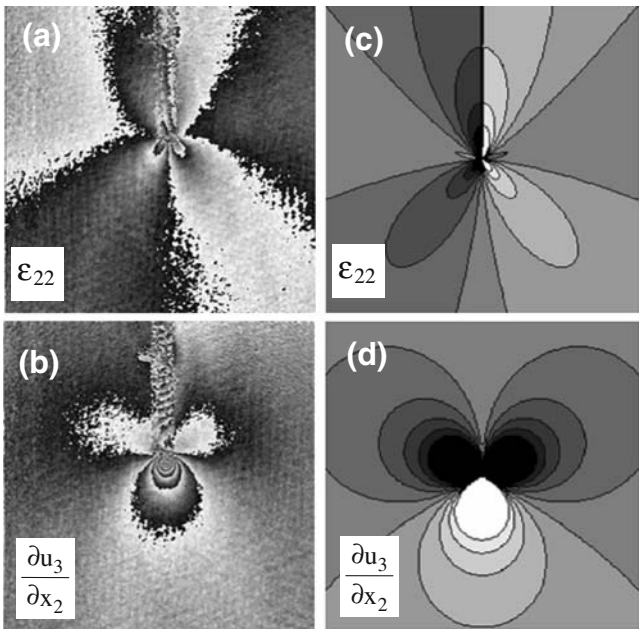

Fig. 13 Crack-tip strain and slope maps corresponding to pure mode-II loading condition (P=550 N, Ψ=90°)

Results: Mode-II and Mixed-Mode Loading Conditions

Crack-tip deformation fields corresponding to a pure mode-II loading condition (P = 550N, Ψ = 90°) and a mixed-mode loading condition (P = 300N, Ψ = 45°) were also obtained using similar procedures. The results from the case of pure mode-II loading are shown in Fig. 13. The resulting ε_{22} strain field is depicted in Fig. 13(a) where each 2π-phase fringe corresponds to a strain difference of 8.36 × 10^{-4}. Figure 13(b) corresponds to the $\frac{\partial u_3}{\partial x_2}$ surface slope field where each 2π-phase fringe represents a slope difference of 3.85 × 10^{-4}. Synthetically generated plots of these quantities, derived by differentiation of the mode-II asymptotic near tip displacement field solutions (31) and (32), are shown to the right of each corresponding field plot.

Results from the mixed-mode loading case are displayed in Fig. 14. The resulting ε_{22} strain field is depicted in

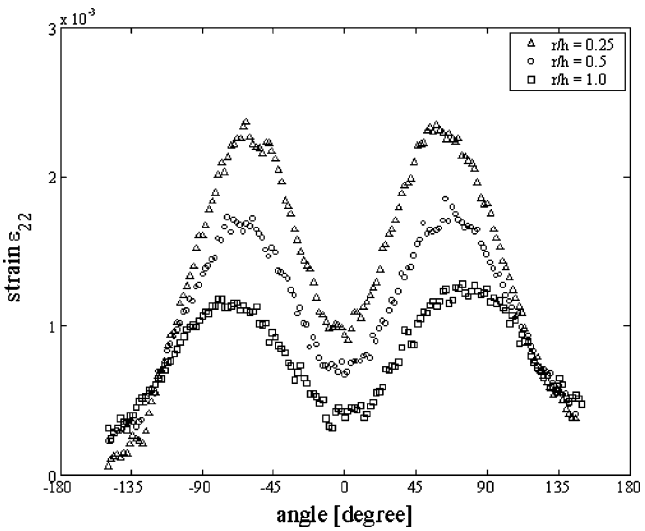

Fig. 12 Angular variations of a strain component ε_{22} around a crack tip for three radii normalized with the specimen thickness h, corresponding to mode-I loading condition

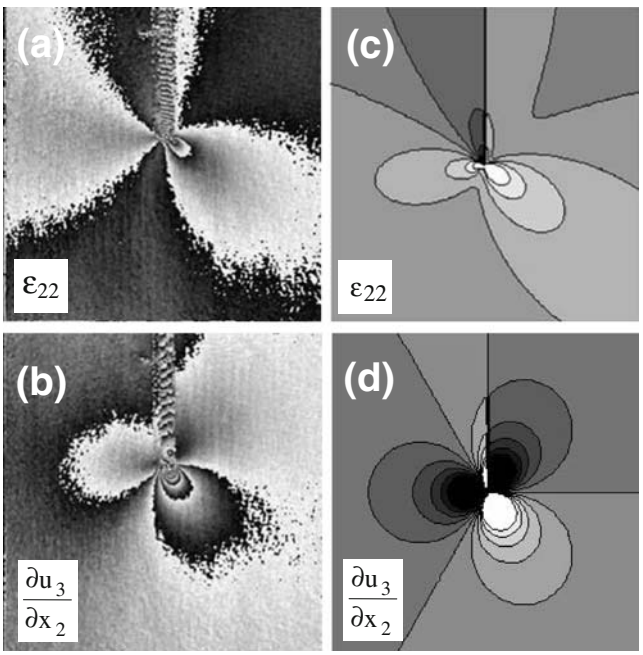

Fig. 14 Crack-tip strain and slope maps corresponding to mixed-mode loading condition (P=300 N, Ψ=45°)

Fig. 14(a) where each 2π-phase fringe once again corresponds to a strain difference of 8.36×10^{-4}. Figure 14(b) corresponds to the $\frac{\partial u_3}{\partial x_2}$ surface slope field where each 2-phase fringe represents a slope difference of 3.85×10^{-4}. Plots to the right of each image display the corresponding synthetically derived predictions for these two field plots which were obtained through linear superposition of the corresponding mode-I and mode-II solutions. In each case the general shape and overall profile of the measured surface slope and strain fields continue to match qualitatively well with the theoretically predicted profiles. The results also demonstrate that the extended CGS technique can be effectively used to measure deformation fields even in the presence of moderate rigid-body rotations.

Conclusions

The Coherent Gradient Sensor (CGS) has been extended to the optical differentiation of specular diffracted wave fronts leading to the combined whole field measurement of in- and out-of-plane displacement field gradients. The extended capability combines the robust attributes of the CGS lateral wave front shearing technique with the high sensitivity feature of moiré interferometry. Combined displacement field measurements are facilitated through the use of a reflective, fine pitch diffraction grating which is replicated onto the surface of a test specimen. The specimen is illuminated by a pair of obliquely incident beams which are directed along primary 1st order diffraction angles in accordance with the grating pitch. The two superimposed +1 and −1 diffracted beams which emerge normal to the specimen surface are prevented from mutually interfering and are instead directed to a CGS set up where each beam is then independently sheared by a pair of parallel Ronchi gratings. The sheared 1st order wave fronts are transmitted through a spatial filtering arrangement and subsequently imaged onto a CCD camera where the resulting interferogram is recorded. Phase shifting interferometry (PSI) techniques are implemented in order to generate a phase map of each differentiated wave front. Extraction of the otherwise coupled in- and out-of-plane displacement field gradients is subsequently achieved through the addition or subtraction of the two complementary phase maps in a post processing procedure. The technique was validated by applying it to the measurement of deformation fields in the vicinity of a notch tip subject to mode-I, mode-II, and mixed mode loading conditions. In each of these cases, the resulting whole field surface slope and strain field profiles were shown to be in good agreement with the theoretically predicted profiles. The results further demonstrated that the technique is capable of accurately measuring deformation fields even in the presence of moderate rigid-body rotations. Future work will consider the application of this technique to dynamic testing applications.

Acknowledgements The authors gratefully acknowledge the support of the US Department of Energy (Grant DE-FG52-06NA 26209, ASC grant B523297 (LLNL), and the Office of Naval Research through a Caltech MURI grant, N0014-06-1-0730—Dr. Y.D.S Rajapakse, Program Manager.

References

1. Tippur HV, Krishnaswamy S, Rosakis AJ (1991) A Coherent Gradient Sensor for crack tip deformation measurements—analysis and experimental results. Int J Fract 48(3):193–204.
2. Tippur HV, Krishnaswamy S, Rosakis AJ (1991) Optical mapping of crack tip deformations using the methods of transmission and reflection Coherent Gradient Sensing—a study of crack tip K-dominance. Int J Fract 52(2):91–117.
3. Tippur HV (1992) Coherent gradient sensing: a Fourier optics analysis and applications to fracture. Appl Opt 31:4428–4439.
4. Tippur HV, Rosakis AJ (1991) Quasi-static and dynamic crack growth along bimaterial interfaces: A note on crack-tip field measurements using coherent gradient sensing. Journal of Experimental Mechanics 31:243–251.
5. Bruck HA, Rosakis AJ (1992) On the sensitivity of coherent gradient sensing: Part I—A theoretical investigation of accuracy in fracture mechanics applications. Opt Lasers Eng 17:83–101.
6. Bruck HA, Rosakis AJ (1993) On the sensitivity of coherent gradient sensing: Part II—An experimental investigation of accuracy in fracture mechanics applications. Opt Lasers Eng 18:25–51.
7. Rosakis AJ (1993) Two optical techniques sensitive to gradients of optical path difference: The method of caustics and the Coherent Gradient Sensor (CGS). In: Epstein J (ed) Experimental Techniques in Fracture, Chapter 10. Wiley, New Jersey.
8. Rosakis AJ (1993) Application of Coherent Gradient Sensing (CGS) to the investigation of dynamic fracture problems. Shukla A, Guest (eds) Special Issue of Optics and Lasers in Engineering devoted to Photomechanics Applied to Dynamic Response of Materials, pp 19, 3–41
9. Lee YJ, Lambros J, Rosakis AJ (1996) Analysis of Coherent Gradient Sensing (CGS) by Fourier optics. Opt Lasers Eng 25:25–53.
10. Shukla A (2006) Dynamic fracture mechanics, 1st edn. World Scientific, Singapore, p 162.
11. Krishnaswamy S, Tippur HV, Rosakis AJ (1992) Measurement of transient crack-tip deformation fields using the method of Coherent Gradient Sensing. J Mech Phys Solids 40:339–372.
12. Mason JJ, Lambros J, Rosakis AJ (1992) The use of a Coherent Gradient Sensor in dynamic mixed-mode fracture mechanics experiments. J Mech Phys Solids 40:641–661.
13. Liu C, Lambros J, Rosakis AJ (1993) Highly transient elastodynamic crack growth in a bimaterial interface: higher order asymptotic analysis and optical experiments. J Mech Phys Solids 41:1887–1954.
14. Lambros J, Rosakis AJ (1995) Dynamic decohesion of bimaterials: experimental observations and failure criteria. Int J Solids Struct 32:2677–2702.
15. Coker D, Rosakis AJ (2001) Experimental observation of intersonic crack growth in asymmetrically loaded unidirectional composites. Philos Mag A 81:571–595.

16. Rosakis AJ, Singh RP, Tsuji Y, Kolawa E, Moore NR Jr (1998) Full field measurements of curvature using Coherent Gradient Sensing: application to thin film characterization. Thin Solid Films 325:42–54.
17. Singh RP, Rosakis AJ (2001) Determination of the yield properties of thin films using enhanced Coherent Gradient Sensing. Journal of Experimental Mechanics 41(4):403–411.
18. Lee H, Rosakis AJ, Freund LB (2001) Full field optical measurement of curvatures in ultra-thin-film-substrate systems in the range of geometrically nonlinear deformations. J Appl Phys 89:6116–6129.
19. Park T-S, Suresh S, Rosakis AJ, Ryu J (2003) Measurement of full-field curvature and geometrical instability of thin film-substrate systems through CGS interferometry. J Mech Phy Solids 51(11–12):2191–2211.
20. Brown MA, Park T-S, Rosakis A, Ustundag E, Huang Y, Tamura N, Valek B (2006) A comparison of X-ray micro diffraction and Coherent Gradient Sensing in measuring discontinuous curvatures in thin film—substrate systems. Journal of Applied Mechanics—Transactions of the ASME 73(5):723–729.
21. Rosakis AJ, Xia K, Lykotrafitis G, Kanamori H (2007) Dynamic shear rupture in frictional interfaces; speeds, directionality, and modes. In: Schubert G (ed) Treatise on Geophysics, volume 4, pp 153–192.
22. Hung YY, Rowlands RE, Daniel IM (1975) Speckle-shearing interferometric technique—full-field strain gauge. Appl Opt 14 (3):618–622.
23. Weissman EM, Post D, Asundi A (1984) Whole-field strain determination by Moiré shearing interferometry. J Strain Anal Eng Des 19(2):77–80.
24. Patorski K, Post D, Czarnek R, Guo Y (1987) Real-time optical differentiation for moiré interferometry. Appl Opt 26(10):1977–1982.
25. Creath K (1985) Phase-shifting speckle interferometry. Appl Opt 24(18):3053–3058.
26. Cloud GL (1995) Optical methods of engineering analysis. Cambridge University Press, New York.
27. Malacara D (1992) Optical shop testing. Wiley, New York.
28. Patorski K, Olszak A (1997) Digital in-plane electronic speckle pattern shearing interferometry. Opt Eng 367:2010–2015.
29. Nakadate S, Saito H (1985) Fringe scanning speckle-pattern interferometry. Appl Opt 24(14):2172–2180.
30. Rastogi PK (1996) Measurement of in-plane strains using electronic speckle and electronic speckle-shearing pattern interferometry. J Mod Opt 43(8):1577–1581.
31. Post D, Han B, Ifju P (1994) High sensitivity Moiré: experimental analysis for mechanics and materials. Springer, New York.
32. Kim KS, Clifton RJ, Kumar P (1977) A combined normal and transverse displacement interferometer with an application to impact of Y-cut quartz. J Appl Phys, 48(10):4132–4139.
33. Espinosa HD, Mello M, Xu Y (1997) A variable sensitivity displacement interferometer with application to wave propagation experiments. Journal of Applied Mechanics—Transactions of the ASME 64:123–131.
34. Tada H, Paris PC, Irwin GR (1973) The stress analysis of cracks handbook. Del Research Corp., Hellertown, PA.
35. He MY, Hutchinson JW (2000) Asymmetric four-point crack specimen. Journal of Applied Mechanics—Transactions of the ASME 67(1):207–209.